**Atmospheric
Chemistry
and Physics
Discussions**

Modeling a typical winter-time dust event over the Arabian Peninsula and the Red Sea

S. Kalenderski[1], G. Stenchikov[1], and C. Zhao[2]

[1]Division of Physical Sciences and Engineering, King Abdullah University of Science and Technology, Thuwal, Saudi Arabia
[2]Atmospheric Sciences and Global Change Division, Pacific Northwest National Laboratory, Richland, WA, USA

Correspondence to: S. Kalenderski (stoitchko.kalenderski@kaust.edu.sa)

Discussion Paper | Discussion Paper | Discussion Paper | Discussion Paper

ACPD

12, 26607–26646, 2012

Modeling a typical winter-time dust event

S. Kalenderski et al.

Title Page

Abstract	Introduction
Conclusions	References
Tables	Figures

|◄ | ►|
| ◄ | ► |

Back | Close

Full Screen / Esc

Printer-friendly Version

Interactive Discussion

Abstract

We used WRF-Chem, a regional meteorological model coupled with an aerosol-chemistry component, to simulate various aspects of the dust phenomena over the Arabian Peninsula and Red Sea during a typical winter-time dust event that occurred in January 2009. The model predicted that the total amount of emitted dust was 18.3 Tg for the entire dust outburst period and that the two maximum daily rates were $\sim 2.4\,\mathrm{Tg\,day}^{-1}$ and $\sim 1.5\,\mathrm{Tg\,day}^{-1}$, corresponding to two periods with the highest aerosol optical depth that were well captured by ground- and satellite-based observations. The model predicted that the dust plume was thick, extensive, and mixed in a deep boundary layer at an altitude of 3–4 km. Its spatial distribution was modeled to be consistent with typical spatial patterns of dust emissions. We utilized MODIS-Aqua and Solar Village AERONET measurements of the aerosol optical depth (AOD) to evaluate the radiative impact of aerosols. Our results clearly indicated that the presence of dust particles in the atmosphere caused a significant reduction in the amount of solar radiation reaching the surface during the dust event. We also found that dust aerosols have significant impact on the energy and nutrient balances of the Red Sea. Our results showed that the simulated cooling under the dust plume reached $100\,\mathrm{W\,m}^{-2}$, which could have profound effects on both the sea surface temperature and circulation. Further analysis of dust generation and its spatial and temporal variability is extremely important for future projections and for better understanding of the climate and ecological history of the Red Sea.

1 Introduction

Mineral dust produced by wind erosion is an important factor in the earth-atmosphere-ocean system. It directly affects the earth's energy budget (Ackermann and Chung, 1992; Seinfeld et al., 2004; Ge et al., 2010; Zhao et al., 2011) by scattering and absorbing radiation; it indirectly affects the energy budget by modifying the microphysics

of the clouds (Satheesh and Moorthy, 2005; Haywood and Boucher, 2000). Mineral dust makes important contributions to the fertilization of phytoplankton through ocean deposition and thus to carbon dioxide levels in the atmosphere (Watson et al., 2000; Johnson et al., 2011). Additionally, dust has substantial impacts on the hydrological cycle (Miller et al., 2004; Zhao et al., 2011, 2012) and many biogeochemical cycles by providing reaction sites and carrying many condensed and absorbed species (Dentener et al., 1996; Huebert et al., 2003).

The MENA region (Middle East and North Africa) is the world's major dust source and accounts for about half of global dust emissions (Prospero et al., 2002). On a global scale, total dust emissions are estimated to be in the range of about 1000 to 2000 $Tg yr^{-1}$ (Tegen et al., 2004); the contribution from MENA would thus be about 500 to 1000 $Tg yr^{-1}$. MENA is subject to strong winds that can carry substantial quantities of finer dust particles over huge distances of about 1000 km or more from the source. For example, each summer large amounts of mineral dust from the Arabian Peninsula and North Africa are transported across the Northern Indian Ocean (Li and Ramanathan, 2002) while dust from the Sahara may reach North America (McKendry et al., 2007). Saharan dust is also a major source of the dust deposited into the Mediterranean Sea and neighboring countries (Santese et al., 2007; Avila et al., 1997). Because of the great distances over which dust plumes can be transported and the large amount of dust injected into the atmosphere, MENA dust has global implications in terms of climate change and biogeochemical cycling. Although much work has investigated the impact of MENA dust on the global scale and on the regional scale over West North Africa (WNA), little has been done to investigate dust transport within the MENA region and its regional impact over the Arabian Peninsula, Red Sea and East North Africa (ENA).

Numerical models allow us to integrate our knowledge of various atmospheric processes and to study their interactions. In this study, we used the Weather Research and Forecast model (Skamarock et al., 2008) coupled with the chemistry module (WRF-Chem; Grell et al., 2005) to investigate dust transport from the Arabian Peninsula

across the Red Sea and the regional impact of dust aerosols. The model results of a dust event that occurred in January 2009 were compared with ground-based Aerosol Robotic Network (AERONET, Holben et al., 1998) measurements and satellite-based Moderate Resolution Imaging Spectroradiometer (MODIS, Salomonson et al., 1989)

5 observations.

The remainder of this paper is organized as follows. In Sect. 2, we present the model description and describe the experimental domain. Section 3 describes the ground- and satellite-based observations. Dust emissions, spatial and vertical distributions, optical properties and heating rates, impact of dust on the radiative budget, surface heat

10 fluxes and temperature, deposition as well as the impact of dust on the Red Sea are discussed in the Sect. 4. Finally, we summarize our work and draw conclusions in the Sect. 5.

2 Model

2.1 Model description

15 The WRF model is a state-of-the-art numerical weather prediction system designed to simulate atmospheric processes for both research and operational applications (Skamarock et al., 2008). The model has been used to simulate atmospheric processes over a wide range of spatial and temporal scales. WRF is based on fully compressible nonhydrostatic Navier-Stokes equations that describe atmospheric flow. The model

20 uses a generalized vertical terrain-following coordinate system and takes into account a variety of physical processes such as boundary layer meteorology, deep and shallow convection, radiation, and land surface processes.

WRF-Chem is an extended version of the WRF model that includes a chemistry component (Grell et al., 2005) and has been widely used for air quality and regional

25 climate studies (Fast et al., 2006, 2009; Zhao et al., 2010, 2011, 2012; Zhang et al., 2009). The chemistry component is fully coupled with the meteorological model and

Title Page

Abstract | Introduction

Conclusions | References

Tables | Figures

◀ | ▶

◀ | ▶

Back | Close

Full Screen / Esc

Printer-friendly Version

Interactive Discussion

both components use the same transport scheme, itegration grid, physics parame-
terizations, and time steps. Additionally, the chemistry component takes into account
a variety of coupled physical and chemical processes such as transport, deposition,
chemical transformations, aerosol interactions, photolysis, radiation, and emissions.

2.2 Model configuration and experimental domain

The WRF framework comprises various parameterizations of unresolved sub-grid-
scale physical processes, which allow the model to be used over a wide range of spatial
and temporal scales. In this study, we have chosen the Mellor-Yamada-Janjic (MYJ)
(Janjic, 2002) planetary boundary layer scheme to parameterize the boundary layer
processes. We selected the Rapid Radiative Transfer Model (RRTM) (Mlawer et al.,
1997) to represent longwave and shortwave radiation transfer within the atmosphere
and the surface. In the model, the Lin microphysics scheme (Lin et al., 1983) accounts
for non-convective precipitation processes and the Grell convective scheme (Grell and
Devenyi, 2002) captures cumulous cloud parameterizations. The NOAH Land Surface
model (Chen and Dudhia, 2001) and the Janjic Eta surface layer scheme (Janjic, 1996)
provide surface process calculations. Additionally, National Centers for Environmental
Prediction's (NCEP) global final analysis (FNL) is used to prepare the lateral boundary
and initial conditions for the meteorological fields and NCEP's daily global sea surface
temperature (SST) analysis (RTG_SST_HR) is used to update SST every six hours.

Version 3.3.1 of the air quality component WRF-Chem used here was configured with
the RADM2 (Regional Acid Deposition Model 2) photochemical mechanism (Stock-
well et al., 1990), the Fast-J photolysis scheme, and the MADE/SORGAM (Modal
Aerosol Dynamics Model for Europe (MADE) and Secondary Organic Aerosol Model
(SORGAM)) aerosol model (Ackerman et al., 1998; Schell et al., 2001). Initial and
boundary conditions for aerosol and gas-phase species were from the default WRF-
Chem profiles. These WRF-Chem profiles were obtained from various field stud-
ies to represent clean atmosphere, maritime, mid-latitude conditions (McKeen et al.,
2002). Anthropogenic emissions were provided by the REanalysis of the TROpospheric

Title Page

Abstract | Introduction

Conclusions | References

Tables | Figures

◄ | ►

◄ | ►

Back | Close

Full Screen / Esc

Printer-friendly Version

Interactive Discussion

(RETRO) chemical composition inventories (http://retro.enes.org/index.shtml) and by the Emission Database for Global Atmospheric Research (EDGAR, http://edgar.jrc.ec. europa.eu). Biomass burning emissions were obtained from the Global Fire Emissions Database, Version 2 (GFEDv2.1) (Randerson et al., 2005) with a 1° × 1° spatial resolution and an 8-day temporal resolution. All emission inventories were preprocessed by the PREP-CHEM-SRC v1 emissions preprocessor (Freitas et al., 2011). Biogenic emissions were not included in this study. Additionally, the GOCART dust emission scheme was coupled with the MADE/SORGAM aerosol model to account for the dust emission processes. The GOCART scheme (Ginoux et al., 2001) calculates the dust emission flux for particle size class p by the expression:

$$F_p = \begin{cases} CSs_p u_{10m}^2 (u_{10m} - u_t) & \text{if} \quad u_{10m} > u_t \\ 0 & \text{otherwise} \end{cases}, \tag{1}$$

where C is an empirical proportionality constant, S is the source function, u_{10m} is the horizontal wind speed at the altitude of 10 m, u_t is the threshold velocity, which is function of particle size, air density, and surface moisture, s_p is the fraction of each size class of dust in the emission. For this simulation, the value of C was tuned to $0.4 \times 10^{-9}\,\text{kg}\,\text{s}^2\text{m}^{-5}$ to be consistent with measurements at the Solar Village AERONET station, located in the eastern part of Saudi Arabia. For details describing the GOCART dust emission scheme in WRF-Chem and selecting the value of C, see Zhao et al. (2010).

The experimental domain covered the Arabian Peninsula, the Red Sea, and eastern part of North Africa, an area from 30° E to 60° E in longitude and from 5° N to 32° N in latitude centered at (18° E, 45° N), with 330 × 297 grid points, a 10 km horizontal resolution, and 40 vertical layers up to 10 hPa. The simulation was performed for a period extending from 1 to 20 January 2009, which included several major dust outbreaks from the Arabian Peninsula across the Red Sea. The impact from the initial conditions was reduced by applying a six-day spin-up period and simulated results only from 7 to

Modeling a typical winter-time dust event

S. Kalenderski et al.

Title Page

Abstract	Introduction
Conclusions	References
Tables	Figures

◀ | ▶

◀ | ▶

Back | Close

Full Screen / Esc

Printer-friendly Version

Interactive Discussion

20 January were used. The radiative impacts were evaluated using two parallel simulations, one including radiative feedback of the dust and the other without it.

3   Observations and measurements

3.1   AERONET data

AERONET is a ground-based remote sensing aerosol network initiated by NASA to measure the optical properties of aerosols and validate satellite retrievals. It uses CIMEL sun and sky radiometers, which are automatic robotically operated instruments located across the world. Aerosol products are routinely retrieved from AERONET raw data following the approach described by Dubovik and King (2000) and Dubovik et al. (2000). In this study, AERONET version 2, level 1.5 cloud-screened data were employed throughout the analysis of the optical properties of aerosols since level-2 quality-assured data were not available. For comparison of the optical properties from the model output at 600 nm wavelength and the AERONET measurements, the Angstrom power law was used:

$$X(600) = X(675) \times \left(\frac{600}{675}\right)^{-\alpha}, \tag{2}$$

where α is the Angstrom exponent provided by the AERONET measurements and given by

$$\alpha = \ln\left(\frac{X(440)}{X(675)}\right) \Big/ \ln\left(\frac{675}{440}\right) \tag{3}$$

and X is an aerosol optical property. Simulated data were taken on the same time basis as the measurements.

Modeling a typical winter-time dust event

S. Kalenderski et al.

Title Page

Abstract	Introduction
Conclusions	References
Tables	Figures

◄◄   ►►

◄   ►

Back   Close

Full Screen / Esc

Printer-friendly Version

Interactive Discussion

3.2 MODIS data

MODIS is a multidisciplinary instrument on board the NASA Terra and Aqua satellites (Salomonson et al., 1989) designed to measure biological and physical processes including clouds and aerosols in the atmosphere, land coverage, sea surface temperature, etc. Polar orbiting MODIS instruments view the entire Earth's surface every one to two days, acquiring data from a large spectral range (36 channels between 405 and 14 385 nm), with high spatial resolution (250 m at the nadir), and across a wide swath (2330 km). The channels between 400 and 2100 nm are suitable for retrieving aerosol properties. The MODIS aerosol products are derived operationally based on three independent algorithms (Remer et al., 2008), two of which derive aerosol properties over land and the other over the ocean. The standard land algorithm is based on the "dark target" approach (King et al., 1992; Kaufman et al., 1997) and consequently does not retrieve aerosol information over bright surfaces such as deserts, ice, and snow. The second land algorithm, "Deep Blue" (Hsu et al., 2004), alleviates the bright-surface problem by employing radiance measurements from the blue channels to infer the properties of aerosols. Its results are therefore used in this study. Deep Blue (Collection 051) daily, level 2, data, available only from MODIS on the Aqua satellite, are used in combination with the standard ocean algorithm (Tanre et al., 1997) for comparison with simulated aerosol properties.

4   Results and discussion

An image of the Red Sea taken by the Aqua MODIS satellite at 10:55 UTC on 14 January and the WRF-Chem predicted dust load field for 11:00 UTC on 14 January are shown in Fig. 1. For the comparison between the satellite observations and simulations, the model domain (Fig. 1, right panel) was spatially restricted to match the region covered by the MODIS image. The clear MODIS image (Fig. 1, left panel) presents a rare opportunity to use visual confirmation to conduct model analysis of mineral dust

transport from the Arabian Peninsula across the Red Sea. Figure 1 confirms that the model correctly simulated the spatial pattern of dust plume over the Red Sea. In addition, since the wind field is the main factor in the calculation of dust emissions, we also compared the modeled 10 m wind speed with the 10 m wind field from ECMWF (European Center for Medium-Range Weather Forecast) Interim global reanalysis. This comparison (not shown) suggests that the two wind fields were in a good agreement most of the time.

4.1 Modeling the distribution of dust

4.1.1 Emission rates

Dust emissions are calculated interactively from Eq. (1) using surface feature data and predictions of surface winds as described by Bagnold et al. (1941). Figure 2 shows the spatial distribution of dust emission fluxes (upper panel) averaged over the simulation period. The emitted total dust amount was 18.3 Tg for the entire domain and simulation period. The similarity between the spatial distribution of the emissions and the prescribed source function, S, as shown in Fig. 2 (middle panel), indicates the dominate role of S in Eq. (1). The most intense dust emissions are simulated to be within the basin of the Arabian Desert, which includes the great An-Nafud Sand Sea (north), the Rub Al Khali desert (south), and the Ad-Dahna desert (middle section to the east). It can also be seen that the dust source region between 22° N to 25° N and about 50 km wide along the west coast of the Arabian Peninsula could potentially play an important role in the dust outflow from the Arabian Peninsula across the Red Sea. Daily simulated dust emissions over the entire domain are also reported in Fig. 2 (lower panel). The emission scheme (1) captures two major dust events on 14 January and 18 January with maximum daily emissions of ~ 2.4 Tg and ~ 1.5 Tg, respectively. The dust event on 14 January is more intense and was partially captured by MODIS satellite observations (Fig. 1, left panel) and the event on 18 January was well captured (will be shown in Sect. 4.2) by the Solar Village AERONET site. Interestingly, these values are

comparable with those reported by Laurent et al. (2006) on daily dust emissions over the Taklimakan desert area in Northwestern China.

4.1.2 Spatial distributions of dust

The MADE/SOGRAM aerosol model is based on a modal representation of the aerosol size distribution in which the total mass is divided in three modes: nucleation, accumulation, and coarse. The lognormal distribution is assumed within each mode and it is given by

$$n\left(\ln d_{\mathrm{p}}\right) = \frac{N}{\sqrt{2\pi}\ln\sigma_{\mathrm{g}}}\exp\left\{-\frac{1}{2}\frac{\left(\ln d_{\mathrm{p}} - \ln d_{\mathrm{g}}\right)^2}{\ln^2\sigma_{\mathrm{g}}}\right\}, \tag{4}$$

where N is the number concentration (m^{-3}), d_{p} is the particle diameter, d_{g} is the median diameter, and σ_{g} is the standard deviation of the distribution. While the standard deviation values, σ_{g}, are prescribed (1.7, 2.0, 2.5), the mean diameter values, d_{g}, are updated from the predicted aerosol mass and number concentrations. The emitted dust particles are distributed in the accumulation and coarse modes with the mass fraction coefficients equal to 7 % and 93 %, respectively. Figure 3 shows the daytime mean spatial distribution of the dust mass concentration in the lower atmosphere (< 1 km AGL) during the simulation period. The coarse mode is shown in the top panel; the accumulation mode in the middle panel; and the total concentration in the bottom panel. In general, the spatial distribution of the dust mass concentration is consistent with the spatial patterns of dust emissions shown in Fig. 2. While the predictions for the coarse and accumulation modes are similar over the Red Sea, the coarse mode is mostly responsible for the dust loading over the regions with the highest dust concentrations, including the middle part of East North Africa, Rub Al Khali, and eastern coast of the Arabian Peninsula.

Figure 4 shows three vertical cross-sections of the dust concentration averaged over the simulation period and their geographic locations. The dust layer is thick, extensive,

and mixed up in a deep boundary layer up to 3–4 km altitude, which facilitates long-range transport over the entire domain. The dust plume over the Red Sea is formed by two major dust source regions along the east and west coast of the Arabian Peninsula as observed above. The dust plume that is formed over the east coast of the Arabian Peninsula and the Rub Al Khali region moves northwest and is mixed with the dust plume that is formed along the east coast of Red Sea, resulting in marked dust events over the Red Sea. The longitude-height cross-section of dust at 13° N (top left panel) reveals that the dust transport could be largely limited because of the blocking effect of the steep mountains along the coast of Red Sea in this part of the basin. Moving northward, the vertical dust cross-section at 23° N (top right panel) indicates that the height of the dust plume reaches beyond 3 km and that the thickness of the dust layer tapers off away from the peninsula due to deposition processes. The last east-west dust cross-section at 27° N (bottom left panel) indicates that the dust plume formed over the west coast of the peninsula is the primary contributor to the dust field over the Red Sea. However, dust transport from the peninsula over the Arabian Sea is extensive at that latitude. Similar results were reported by Papayannis et al. (2005) who reported the vertical distributions of Sahara dust aerosols over the Northeastern Mediterranean region as observed by two LIDAR systems during a typical dust outbreak in August 2000.

4.2 The optical properties and heating rates of dust

A parameterization (Ghan and Zaveri, 2007) of the Mie theory is employed in WRF-Chem to calculate the optical properties of aerosols, such the extinction coefficient, the single scattering albedo, and the asymmetry factor required by the radiative transfer model. The parameterization is modified for the sectional representation of the aerosol size distribution (Fast et al., 2006; Barnard et al., 2010) and is relatively efficient computationally and general enough to account for the variability in aerosol composition, size distribution, and ambient relative humidity, which are difficult to capture using the common method of lookup tables. The effects of water uptake and the internal mixture

Full Screen / Esc

Printer-friendly Version

Interactive Discussion

are treated as a variation of the particle wet diameter (d_w) and the wet refractive index (n_w). The wet diameter can be obtained from the dry mode diameter by accounting for the relative humidity and the wet refractive index can be obtained from the composition of the aerosol particles and the complex refractive index of each component. Once d_w and n_w are calculated, an aerosol optical property (P) is parameterized as

$$P = \exp\left(\sum_{k=0}^{4} A_k(n_w)T_k(x)\right),\qquad(5)$$

where

$$x = \frac{2\log(d_w) - \log(d_{min}) - \log(d_{max})}{\log(d_{max}) - \log(d_{min})},\qquad(6)$$

$T_k(x)$ is the Chebyshev polynomial of order k, and A_k are the Chebyshev coefficients interpolated bilinearly from a table of coefficients. The table of coefficients is calculated by fitting the Chebyshev polynomials to a set of full Mie calculations performed once at the beginning of the simulation. Later, only Eq. (6) is used to calculate the optical properties of the aerosols.

4.2.1 Aerosol Optical Depth (AOD)

Aqua-MODIS observations have limited special and temporal coverage over the modeled domain. The available observations usually cover a small part of the domain twice per day (day and night). These limitations plus cloudiness make comparisons of the MODIS and simulated data difficult on the time scale of the simulation period (a few weeks). Figure 5 shows the simulated AOD (600 nm) at 11:00 UTC on 14 January 2009, in comparison with two MODIS retrievals (550 nm) at 10:00 and 10:55 UTC on 14 January 2009, observations taken during the integration period. The MODIS retrievals are a combination of the standard ocean and Deep Blue products. The observed MODIS AOD values compare well to the high optical depth values simulated

Full Screen / Esc

Printer-friendly Version

Interactive Discussion

over the entire domain whenever they are available. Unfortunately, because of clouds and insufficient coverage, very few MODIS observations are available over the Rub Al Khali area, where the predicted AOD values are the highest at that time.

Figure 6 shows the mean spatial distribution of the simulated AOD at 600 nm (upper panel) and a comparison between the hourly calculated AOD and the corresponding AERONET values at the Solar Village site during the simulation period (lower panel). Since AERONET does instantaneous measurements during the daytime, the data were averaged to hourly values for comparison with the simulated AOD values. The mean values of these time series are consistent since the simulated mean value (0.25) was obtained from a sample when the AERONET measurements were available and the observed AERONET mean value (0.28) was used to tune the dust emissions scheme, i.e., the value of the proportionality constant, C. The dust event predicted by WRF-Chem on 18 January 2009 is verified by the observed AOD measurements at the Solar Village station and generally the two time series correlate well with each other most of the time. The mean spatial distribution of the simulated AOD (upper panel) is consistent with the climatology values and spatial patterns reported by Ginoux et al. (2001) and Prospero et al. (2002) for this region and this time of the year with the highest AOD over the Rub Al Khali region.

4.2.2 Heating Rates of Aerosols

The rate of change of temperature in a layer, known as the aerosol heating rate, depends on the optical properties and vertical distribution of the aerosols. The heating rate may therefore vary significantly from one region to another. Zhao et al. (2011) analyzed the sensitivity of heating rates simulated by WRF-Chem to dust absorption properties by using different values for the imaginary part of the dust refractive index. In this study, the imaginary part of the dust refractive index is not wave-dependent and set to 0.006 (strongly absorbing dust), which gives comparable results with some other studies and is within the range of uncertainty observed in the AERONET values for the Solar Village site and this particular period of simulation. Uncertainties on the

imaginary part of the dust refractive index retrieved from AERONET observations are 50 % as reported by Dubovic et al. (2002). Figure 7 presents the vertical profiles of the dust induced perturbations in solar heating rates averaged during the simulation period at 10:00 UTC over the Solar Village station. It is apparent that the presence of dust in the lower atmosphere leads to a significant increase in the shortwave heating rates. The peak heating rate at 10 UTC is found at about 1.2 km with a mean value of 1.68 K day^{-1}. Above this altitude, the solar heating rate perturbations gradually decrease to become insignificant at 5 km. In comparison, Zhao et al. (2010) modeled the mean daytime dust heating profiles with maximum rates up of 0.7 K day^{-1} in January 2006 at Niamey Airport in Niger, Africa. Liu et al. (2011) reported maximum daily heating rates of 2.74 K day^{-1} and 1.91 K day^{-1} for two dust events that occurred in southeast China during 14–17 March and 25–26 April 2009. The mean simulated SSA (600 nm) value over the Solar Village was 0.98, which is comparable to the value of 0.99 ± 0.01 reported by Osborne et al. (2008) for Saharan dust. The warming effect of the dust layer aloft and cooling at the surface could affect the stability and turbulent mixing of the lower atmosphere and thus the boundary layer properties.

4.3 Radiative forcing from dust

4.3.1 The impact of dust on the radiation budget

The impact of dust on the radiation budget is determined from the difference between the net radiative fluxes obtained in two parallel simulations at the surface (SFC) and the top of the atmosphere (TOA) as follows:

$$\Delta F_{SFC} = F_{SFC}^{w} - F_{SFC}^{o}$$
$$\Delta F_{TOA} = -(F_{TOA}^{w} - F_{TOA}^{o}), \tag{7}$$

where F is the net radiative flux, which is the difference between the downward ($F\downarrow$) and upward ($F\uparrow$) fluxes:

$$F = F\downarrow - F\uparrow, \tag{8}$$

and (w) and (o) indicate radiative fluxes with and without radiative feedback, respec-
tively. This convention is used both for longwave (LW) and shortwave (SW) radiation
and a negative sign implies an overall cooling effect whereas a positive sign implies
an overall heating effect. It should also be noted that the downward SW flux is the
dominant component in the net flux calculations at the surface and that the upward
SW flux is the dominant component at the TOA. We below consider the dust effect for
clear sky conditions and call it radiative forcing, although, strictly speaking, it includes
atmospheric and surface temperature responses.

Figure 8 shows the spatial distribution of the clear sky daily averaged SW (upper
row), LW (middle row), and total (lower row) radiative effects from dust at the sur-
face (left column) and at the TOA (right column). As shown in the figure, SW radiative
forcing at the surface is negative almost everywhere with a domain averaged value
of $-6.0\,\mathrm{W\,m^{-2}}$ and a maximum of $-19.2\,\mathrm{W\,m^{-2}}$. Comparable values for SW radiative
forcing at the surface were found by Han et al. (2011). In their work, the reported
monthly averaged values, obtained with the RAMS-CMAQ model, ranged from -12 to
$-8\,\mathrm{W\,m^{-2}}$ for East Asia. McFarlane et al. (2009) reported 24-h averaged SW instanta-
neous surface aerosol radiative forcing of $-21.1 \pm 14.3\,\mathrm{W\,m^{-2}}$ at Niamey, Niger, during
2006. Finally, Satheesh et al. (2006) estimated the daily averaged surface radiative
forcing over the Arabian Sea to be from -16.2 to $-5.5\,\mathrm{W\,m^{-2}}$ during the winter mon-
soon season. The LW radiative forcing at the surface (middle row) has the opposite
response to SW forcing; i.e., the elevated dust layer increases LW radiation at the sur-
face, causing overall warming with a domain averaged value of $1.7\,\mathrm{W\,m^{-2}}$ and a max-
imum of $6.1\,\mathrm{W\,m^{-2}}$, which are consistent with the values of 0.9–$1.4\,\mathrm{W\,m^{-2}}$ (depending
on the altitude of the dust layer) reported by Liao and Seinfeld (1998). However, the
net radiative effect (lower panel) is dominated by the SW radiative forcing and overall

(land + ocean) is cooling with a domain-averaged value of $-4.3\,\mathrm{W\,m^{-2}}$ and a maximum of $-16\,\mathrm{W\,m^{-2}}$. It should be highlighted here that the instantaneous surface forcing of dust (not shown) can be considerably larger than the daily averaged one. For example, the simulated instantaneous solar radiative forcing at the surface reached up to

5    $-205\,\mathrm{W\,m^{-2}}$ over the Arabian Sea at noon on 14 January 2009 and had a regional mean value of $-14.1\,\mathrm{W\,m^{-2}}$. These results are comparable with results obtained in previous studies: Slingo et al. (2006) reported that the incoming solar fluxes at the surface dropped by $250\,\mathrm{W\,m^{-2}}$ during a major Saharan dust storm; Mallet et al. (2009) simulated a remarkable instantaneous (at midday) decrease in the surface SW radia-

10   tion, with a regional mean of $-137\,\mathrm{W\,m^{-2}}$ and a maximum of $-400\,\mathrm{W\,m^{-2}}$, over West Africa during March 2006.

The right column of Fig. 8 displays the spatial distribution of the simulated clear sky daily averaged SW (upper row), LW (middle row), and total (lower row) radiative effect of dust at TOA. The SW radiative forcing (upper panel) is always negative over the

15   ocean and could be either positive or negative over the land with a domain-averaged value of $-2.3\,\mathrm{W\,m^{-2}}$ and a maximum of $-17.8\,\mathrm{W\,m^{-2}}$. Over oceanic regions, the SW cooling effect at TOA is stronger due to the smaller surface albedo, where the scattering effects dominate and more SW energy is reflected back to space. Over bright surfaces with wide ranges of surface albedo and dust type, scattering (cooling) and absorbing

20   (warming) effects compensate each other, resulting in a smaller SW radiative forcing at TOA. Sensitivity tests reveal that the sign and magnitude of SW instantaneous forcing over the land strongly depend on the solar absorptivity of the dust. Using a half-value of 0.003 (moderate absorbing dust) for the imaginary part of the refractive index creates negative SW forcing over the entire domain including the Rub Al Khali region and

25   decreases the overall domain-averaged effect by a factor of 2, while a value of 0.006 creates positive instantaneous forcing over a large part of the peninsula (not shown). The LW forcing is small and mostly positive with daily mean values between -2.7 and $1.8\,\mathrm{W\,m^{-2}}$ (mean of $0.2\,\mathrm{W\,m^{-2}}$) and it is practically insensitive ($< 4\,\%$) to variations in the imaginary part of the refractive index. The total daily averaged radiative forcing

(lower panel) is generally negative with a domain-averaged value of $-2.1\,\mathrm{W\,m^{-2}}$. There-fore, within the atmosphere, the radiative effect of dust ($\Delta F_{\mathrm{ATM}} = \Delta F_{\mathrm{TOA}} - \Delta F_{\mathrm{SFC}}$) is $2.3\,\mathrm{W\,m^{-2}}$, indicating a heating effect from dust aerosols caused mostly by absorption of solar radiation. For comparison, Ge et al. (2010) calculated a daily averaged SW ra-
5 diative forcing of $0.52 \pm 1.69\,\mathrm{W\,m^{-2}}$ at TOA for Zhangye, which is located in a semi-arid area in northwest China, during the period of late April to mid-June in 2008. Satheesh et al. (2006) simulated the daily averaged SW radiative forcing over the Arabian Sea as ranging from -7.3 to $-6.1\,\mathrm{W\,m^{-2}}$, with the LW forcing from 0.8 to $1.2\,\mathrm{W\,m^{-2}}$, and the total forcing from -6.1 to $-5.2\,\mathrm{W\,m^{-2}}$ at TOA, during the winter monsoon season
10 for 8 yr from 1995 to 2002. Mallet et al. (2009) simulated the instantaneous net cooling effect at TOA with regional mean of $-12.0\,\mathrm{W\,m^{-2}}$ over West Africa during March 2006.

4.3.2 Impact on surface energy budget

WRF-Chem allows online interaction of the simulated dust field with the SW and LW radiation and consequently with the model dynamics. In this section, we investigate the
15 responses of the surface latent heat fluxes (LH), the sensible heat flux (SH), and the two meter temperature (T2) to the radiative forcing of dust. Figure 9 shows the spa-tial distribution of instantaneous (at 12:00 UTC) LH (upper panel), SH (middle panel), and T2 (lower panel) atmospheric responses averaged over the simulation period. The maximum response of the latent heat flux occurs at around 12:00 UTC, about 2–3 h af-
20 ter the maximum dust radiative effect at 10:00 UTC. Simulations indicate that the neg-ative dust surface forcing causes a small overall decrease in the domain-averaged LH of $-0.2\,\mathrm{W\,m^{-2}}$ ($< 1\,\%$), SH of $-6.1\,\mathrm{W\,m^{-2}}$ ($< 5\,\%$), and T2 of $-0.1\,\mathrm{K}$ ($< 1\,\%$). However, as observed in the figure, the variations in LH, SH, and T2 can be locally significant up to $-45.2\,\mathrm{W\,m^{-2}}$, $-45.6\,\mathrm{W\,m^{-2}}$, and $-0.7\,\mathrm{K}$, respectively. In general, sensible heat
25 fluxes are strongly reduced over land surfaces (mostly source regions) caused by a re-duction in the temperature over the land, but with relatively small changes over the ocean, which is because the SST is prescribed in both simulations with and without

dust radiative feedback. However, it should be noted that the dust impact on SST in the short term should be small because of the high heat capacity of the ocean (Zhao et al., 2011).

For comparison, Mallet et al. (2009) reported a surface temperature decrease of about −0.68 K (at noon) averaged over the 9°–17° N, 10° W–20° E region, for 9–12 March 2006 and intense decreases of the sensible heat flux with a maximum of 200 W m^{-2} corresponding to higher dust AOD. Miller et al. (2004) reported a global and annual averaged decrease of −1.13 W m^{-2} in LH and −0.47 W m^{-2} in SH for AGCM experiments. Additionally, they also pointed out that despite its dominant role on the global scale as a compensating mechanism for the dust radiative forcing at the surface, LH may increase locally over arid regions that are sources of dust. This effect is quite consistent with the results shown in the Fig. 9.

4.4 Dust deposition

Dust particles can be removed from the atmosphere by dry and/or wet deposition processes. During the simulation period, there was no precipitation over the region. Dry deposition was therefore the dominant removal process in this study. The dry deposition flux of dust (F_d) is calculated by multiplying the dust concentration (C) in the lowest model layer by the deposition velocity (V_d) for both accumulation and coarse modes as follows:

$$F_d = C_a \times V_{da} + C_c \times V_{dc}, \tag{9}$$

where the subscripts a and c refer to the accumulation and coarse modes, respectively. Dry deposition velocities in WRF-Chem are parameterized based on Binkowski and Shankar (1995). This parameterization takes into account deposition processes such as the turbulent transfer of aerosol particles to the surface, gravitational settling, diffusion, impaction, and interception. Figure 10 (upper panel) shows the spatial distribution of dust deposition rates averaged over the simulation period. The highest deposition rates are found over the source regions with the maximum greater than 450 g m^{-2} yr^{-1}

Full Screen / Esc

Printer-friendly Version

Interactive Discussion

Discussion Paper | Discussion Paper | Discussion Paper | Discussion Paper

at a few isolated locations and a domain-averaged value of $43.3\,\mathrm{g\,m^{-2}\,yr^{-1}}$. The total deposition for the entire domain and simulation period is 14.3 Tg, less than the earlier reported (Sect. 4.1.1) emitted total dust amount of 18.3 Tg. Simulated daily depositions are shown in the lower panel of Fig. 10. Similar to the daily emissions (Fig. 2, lower panel), the dust deposition time series has two peaks as well although there is a lag time of 24 h between the peaks of deposition and emission. For comparison, Zhang et al. (1993) estimated dust dry deposition rates over Huanghai, China (Yellow sea) ranging from $7\,\mathrm{g\,m^{-2}\,yr^{-1}}$ to $42\,\mathrm{g\,m^{-2}\,yr^{-1}}$ in the winter. Another detailed study estimated that the deposition rates over Chinese deserts ranged from $14\,\mathrm{g\,m^{-2}\,yr^{-1}}$ to $2100\,\mathrm{g\,m^{-2}\,yr^{-1}}$ (Zhang et al., 1997). Prospero et al. (1996) modeled dust deposition rates for the Mediterranean sea to be 3–$14\,\mathrm{g\,m^{-2}\,yr^{-1}}$, which were comparable to rates obtained from direct measurements. Finally, global dust deposition fluxes over the ocean calculated by Duce et al. (1991) were $1\,\mathrm{g\,m^{-2}\,yr^{-1}}$ and $1.5\,\mathrm{g\,m^{-2}\,yr^{-1}}$ for dry and wet deposition, respectively, and $2.5\,\mathrm{g\,m^{-2}\,yr^{-1}}$ total.

4.5   The impact of dust on the Red Sea

The dust outbreak on 14 January 2009 considered in this study provides a good opportunity to evaluate the effect of dust plumes on the Red Sea. The direct effect of cross-sea continental air-mass transport, associated with the coastal terrain gaps (e.g., Tokar Gap), on surface currents and air-sea interactions was discussed by Houshuo et al. (2009). They mentioned that such episodes are frequent especially in the winter. However, they did not account for dust transport and its radiative effect. Here, we consider the effect of the simulated aerosol plume on solar surface heating. We also calculate the amount of dust deposited into the sea during the simulation period. Because there is little river discharge with associated chemical and nutrient inflow in the study area, the atmospheric deposition of aerosols and gaseous chemicals to the Red Sea is extremely important to maintaining nutrient and chemical balances.

The right column in Fig. 8 shows that the averaged aerosol radiative effect at TOA is significantly stronger over the Red Sea than over the surrounding desert areas. The aerosols cool the atmospheric column over the Red Sea by up to $20\,\mathrm{W\,m^{-2}}$. This is because the sea has a lower albedo than the desert and because a reflecting aerosol layer has a relatively stronger effect over the dark sea surface. Figure 11 shows the instantaneous distribution of the aerosol loading and associated anomaly of the net radiative solar flux at the surface at 11:00 UTC on 14 January 2009. Just under the aerosol plume, the solar radiance decreased by almost $100\,\mathrm{W\,m^{-2}}$. This should have a profound effect on the energy balance at the sea surface. A complete understanding of the Red Sea's evolution and variability is impossible without a detailed quantification of the radiative effects of aerosols.

It is well known that the Red Sea is extremely oligotrophic in its central deep areas especially in the North, far from the inflow of nutrient-rich waters from the Indian Ocean through the Bab-el-Mandeb Strait. The delivery of nutrients through atmospheric pathways is therefore especially important to the ecosystem of the Red Sea. During the dust outbreak episode considered in this paper, the total deposition of aerosols to the Red Sea reached 0.65 Tg. Dust plumes are frequent in the Northern part of the Red Sea where nutrients are particularly deficient. To quantify nutrient delivery by atmospheric deposition, we plan to run multi-season calculations and produce multi-season and multi-year statistics on nutrient deposition to the Red Sea.

5 Summary and conclusion

We used the WRF-Chem model to investigate a typical dust event over the Arabian Peninsula during January 2009. The model simulated the most intense dust emissions over the basin of the Arabian Desert with the total amount of 18.3 Tg for the entire dust outburst period of 14 days and two daily maximums of ~ 2.4 Tg and ~ 1.5 Tg, which corresponded to two periods with the highest AOD captured by AERONET and MODIS instruments. The predicted dust plume was thick, extensive, and mixed up in a deep

Full Screen / Esc

Printer-friendly Version

Interactive Discussion

boundary layer of 3–4 km height, which was suitable for long-range transport over the entire study domain and, in general, its spatial distributions were consistent with the spatial patterns of dust emissions.

MODIS-Aqua and Solar Village AERONET measurements of AOD and SSA have been used to evaluate the spatial distribution and optical thickness of the aerosol layer calculated by WRF-Chem. The observed MODIS AOD values compared well with the high optical depth values simulated over the entire domain when available. However, because of clouds and the poor spatial and temporal coverage (twice per day) of the domain, further comparisons were difficult on time scale of the simulation period. On the other hand, simulated and observed AERONET hourly measurements of AOD at 600 nm were similar on most days during the period with average values of 0.28 and 0.25, respectively. The maximum of the simulated mean dust heating rates at a mean SSA (600 nm) value of 0.98 over the Solar Village reached 1.68 K day^{-1} at a height of 1.2 km. Above this altitude, the heating rate perturbations gradually decreased to become insignificant at 5 km. In general, for accurate assessments of the predicted optical properties of aerosols over the modeled region, more observations would be required along with a better understanding of dust phenomena as a whole.

Our results clearly indicate that the presence of dust particles in the atmosphere causes a significant reduction in solar radiation reaching the surface with an instantaneous (daily) regional mean value of -14.1 W m^{-2} (-6.0 W m^{-2}) and a maximum of -205 W m^{-2} (-19 W m^{-2}). The simulated net radiative effect at the top of the atmosphere (TOA) was small with a daily domain-averaged value of -2.1 W m^{-2}, indicating cooling of the earth-atmosphere system. The longwave radiative forcing of dust at the bottom of the atmosphere was positive and small with a domain averaged value of 1.7 W m^{-2}, which did not change the overall cooling effect on the surface. At TOA, the daily radiative forcing of dust in general is much smaller than that on the surface. The LW forcing at TOA is mostly positive with a regional mean value of 0.2 W m^{-2} and ranging from -2.7 to 1.8 W m^{-2}. The SW forcing at TOA is always negative over the ocean and could be either positive or negative over the land with a domain-averaged value

of $-2.3\,\mathrm{W\,m^{-2}}$. However, the sensitivity test indicates that the sign and magnitude of SW instantaneous forcing over bright surfaces strongly depend on the solar absorptivity of the dust. Using a value of 0.003 (half value of what was used in the main experiments) for the imaginary part of the refractive index creates negative SW forcing over the entire Arabian peninsula including the Rub Al Khali region and decreases the overall domain-averaged effect by a factor of 2. The domain-averaged instantaneous radiative forcing within the atmosphere was $2.3\,\mathrm{W\,m^{-2}}$, indicating a heating effect of dust aerosols caused mostly by absorption of solar radiation.

WRF-Chem allows online interaction of the simulated dust field with the SW and LW radiation and consequently with the model's dynamics. Simulations indicate that the negative surface forcing causes a small overall decrease in the LH of $-0.2\,\mathrm{W\,m^{-2}}\,(<1\,\%)$, SH of $-6.1\,\mathrm{W\,m^{-2}}\,(<5\,\%)$, and T2 of $-0.1\,\mathrm{K}\,(<1\,\%)$. However, the variations in LH, SH, and T2 can be locally significant up to $-45.2\,\mathrm{W\,m^{-2}}$, $-45.6\,\mathrm{W\,m^{-2}}$, and $-0.7\,\mathrm{K}$, respectively. Additionally, the model also calculates dust deposition rates with a domain-averaged value of $43.3\,\mathrm{g\,m^{-2}\,yr^{-1}}$ and the calculated total deposition for the entire domain and simulation period is 14.3 Tg.

Dust plumes produce a profound effect on the thermal and chemical balances of the Red Sea by delivering nutrients through dust deposition, reducing solar heating, and affecting air circulation over the sea. Reducing dust transport might significantly damage the ecosystem of the Red Sea and cause overheating of the sea surface. A detailed analysis of dust generation and its spatial and temporal variability is extremely important for better understanding of the climate, ecological history and future evolution of the Red Sea.

References

Ackermann, F. A. and Chung, H.: Radiative effects of airborne dust and regional energy budget at the top of the atmosphere, J. Appl. Meteor., 31, 223–236, 1992.

Title Page

Abstract | Introduction

Conclusions | References

Tables | Figures

|◄ | ►|

◄ | ►

Back | Close

Full Screen / Esc

Printer-friendly Version

Interactive Discussion

Ackermann, I. J., Hass, H., Memmesheimer, M., Ebel, A., Binkowski, F. S., and Shankar, U.: Modal aerosol dynamics model for Europe: Development and first applications, Atmos. Environ., 32, 2981–2999, 1998.

Avila, A., Queralt-Mitjans, I., and Alarcon, M.: Mineralogical composition of African dust delivered by red rains over Northeastern Spain, J. Geophys. Res., 102, 21977–21996, 1997.

Bagnold, R. A.: The Physics of Blown Sand and Desert Dunes, Methuen, New York, 265 pp., 1941.

Barnard, J. C., Fast, J. D., Paredes-Miranda, G., Arnott, W. P., and Laskin, A.: Technical Note: Evaluation of the WRF-Chem "Aerosol Chemical to Aerosol Optical Properties" Module using data from the MILAGRO campaign, Atmos. Chem. Phys., 10, 7325–7340, doi:10.5194/acp-10-7325-2010, 2010.

Haywood, J. and Boucher, O.: Estimates of the direct and indirect radiative forcing due to tropospheric aerosols: a review, Rev. Geophys., 38, 513–543, 2000.

Hsu, N. C., Tsay, S. C., King, M. D., and Herman, J. R.: Aerosol properties over bright-reflecting source regions, IEEE Trans. Geosci. Remote Sens., 42, 557–569, doi:10.1109/TGRS.2004.824067, 2004.

Huebert, B. J., Russell, B. T., Shi, P. B., Kim, G., Kawamura, Y. J., Carmichael, K., and Nakajima, G.: An overviewof ACE-Asia: strategies for quantifying the relationships between Asian aerosols and their climatic impacts, J. Geophys. Res., 108, 8633, doi:10.1029/2003JD003550, 2003.

Chen, F. and Dudhia, J.: Coupling an advanced land-surface/hydrology model with the Penn State/NCAR MM5 modeling system. Part I: Model description and implementation, Mon. Wea. Rev., 129, 569–585, 2001.

Dentener, F. J., Carmichael, G. R., Zhang, Y., Lelieveld, J., and Crutzen, P. J.: Role of mineral aerosol as a reactive surface in the global troposphere, J. Geophys. Res, 101, 22869–22889, 1996.

Dubovik, O. and King, M. D.: A flexible inversion algorithm for retrieval of aerosol optical properties from sun and sky radiance measurements, J. Geophys. Res., 105, 20673–20696, 2000.

Dubovik, O., Smirnov, A., Holben, B. N., King, M. D., Kaufman, Y. J., Eck, T. F., and Slutsker, I.: Accuracy assessments of aerosol optical properties retrieved from Aerosol Robotic Network (AERONET) Sun and sky radiance measurements, J. Geophys. Res., 105, 9791–9806, 2000.

Title Page

Abstract | Introduction

Conclusions | References

Tables | Figures

|◄ | ►|

◄ | ►

Back | Close

Full Screen / Esc

Printer-friendly Version

Interactive Discussion

Dubovik, O., Holben, B., Eck, T., Smirnov, A., Kaufman, Y., King, M., Tanré, D., and Slutsker, I.: Variability of absorption and optical properties of key aerosol types observed in world-wide locations, J. Atmos. Sci., 59, 590–608, 2002.

Duce, R. A., Liss, P. S., Merrill, J. T., Atlas, E. L., Buat-Menard, P., Hicks, B. B., Miller, J. M., Prospero, J. M., Arimoto, R., Church, T. M., Ellis, W., Galloway, J. N., Hansen, L., Jickells, T. D., Knap, A. H., Reinhardt, K. H., Schneider, B., Soudine, A., Tokos, J. J., Tsunogai, S., Wollast, R., and Zhou, M.: The atmospheric input of trace species to the world ocean, Global Biogeochemical Cycles, 5, 193–259, 1991.

Fast, J. D, Gustafson Jr., W. I., Easter, R. C., Zaveri, R. A., Barnard, J. C., Chapman, E. G., and Grell, G. A.: Evolution of ozone, particulates, and aerosol direct forcing in an urban area using a new fully-coupled meteorology, chemistry, and aerosol model, J. Geophys. Res., 111, D21305, doi:10.1029/2005JD006721, 2006.

Fast, J., Aiken, A. C., Allan, J., Alexander, L., Campos, T., Canagaratna, M. R., Chapman, E., DeCarlo, P. F., de Foy, B., Gaffney, J., de Gouw, J., Doran, J. C., Emmons, L., Hodzic, A., Herndon, S. C., Huey, G., Jayne, J. T., Jimenez, J. L., Kleinman, L., Kuster, W., Marley, N., Russell, L., Ochoa, C., Onasch, T. B., Pekour, M., Song, C., Ulbrich, I. M., Warneke, C., Welsh-Bon, D., Wiedinmyer, C., Worsnop, D. R., Yu, X.-Y., and Zaveri, R.: Evaluating simulated primary anthropogenic and biomass burning organic aerosols during MILAGRO: implications for assessing treatments of secondary organic aerosols, Atmos. Chem. Phys., 9, 6191–6215, doi:10.5194/acp-9-6191-2009, 2009.

Freitas, S. R., Longo, K. M., Alonso, M. F., Pirre, M., Marecal, V., Grell, G., Stockler, R., Mello, R. F., and Sánchez Gácita, M.: PREP-CHEM-SRC – 1.0: a preprocessor of trace gas and aerosol emission fields for regional and global atmospheric chemistry models, Geosci. Model Dev., 4, 419–433, doi:10.5194/gmd-4-419-2011, 2011.

Ge, J. M., Su, J., Ackerman, T. P., Fu, Q., Huang, J. P., and Shi, J. S.: Dust aerosol optical properties retrieval and radiative forcing over Northwestern China during the 2008 China-U.S. joint field experiment, J. Geophys. Res., 115, D00K12, doi:10.1029/2009JD013263, 2010.

Ghan, S. J. and Zaveri, R. A.: Parameterization of optical properties for hydrated internally mixed aerosol, J. Geophys. Res., 112, D10201, doi:10.1029/2006JD007927, 2007.

Ginoux, P., Chin, M., Tegen, I., Prospero, J. M., Holben, B., Dubovik, O., and Lin, S.: Sources and distributions of dust aerosols simulated with the GOCART model, J. Geophys. Res., 106, 20225–20273, 2001.

Grell, G. A. and Devenyi, D.: A generalized approach to parameterizing convection combining ensemble and data assimilation techniques, Geophys. Res. Lett., 29, 1693, doi:10.1029/2002GL015311, 2002.

Grell, G. A., Peckham, S. E., Schmitz, R., McKeen, S. A., Frost, G., Skamarock, W. C., and Eder, B.: Fully coupled "online" chemistry within the WRF model, Atmos. Environ., 39, 6957–6975, 2005.

Han, X., Zhang, M., Han, Z., Xin, J., and Liu, X.: Simulation of aerosol direct radiative forcing with RAMS-CMAQ in East Asia, Atmos. Environ., 45, 6576–6592, doi:10.1016/j.atmosenv.2011.08.006, 2011.

Holben, B. N., Eck, T. F., Slutsker, I., Tanré, D., Buis, J. P.,Stezer, A., Vermote, E., Reagan, Y., Kaufman, U. J., Nakajima, T., Lavenu, F., Jankowiak, I., and Smirnov, A.: AERONET-A federated instrument network and data archive for aerosol characterization, Remote Sens. Environ., 66, 1–16, 1998.

Janjic, Z. I.: The surface layer in the NCEP Eta Model, Eleventh Conference on Numerical Weather Prediction, Norfolk, VA, 19–23 August 1996; Amer. Meteor. Soc., Boston, MA, 354–355, 1996.

Janjic, Z. I.: Nonsingular Implementation of the Mellor-Yamada Level 2.5 Scheme in the NCEP Meso model, NCEP Office Note, No. 437, 61 pp., http://www.emc.ncep.noaa.gov/officenotes/newernotes/on437.pdf, 2001.

Jiang, H., Farrar, J. T., Beardsley, R. C., Chen, R., and Chen, C.: Zonal surface wind jets across the Red Sea due to mountain gap forcing along both sides of the Red Sea. Geophys. Res. Lett., 36, L19605, doi:10.1029/2009GL040008, 2009.

Johnson, M. S., Meskhidze, N., Kiliyanpilakkil, V. P., and Gassó, S.: Understanding the transport of Patagonian dust and its influence on marine biological activity in the South Atlantic Ocean, Atmos. Chem. Phys., 11, 2487–2502, doi:10.5194/acp-11-2487-2011, 2011.

King, M. D., Kaufman, Y. J., Menzel, W. P., and Tanre, D.: Remote sensing of cloud, aerosol, and water vapor properties from the Moderate Resolution Imaging Spectrometer (MODIS), IEEE Trans. Geosci. Remote Sensing, 30, 1–27, 1992.

Kaufman, Y. J., Tanre, D., Remer, L. A., Vermote, E. F., Chu, A., and Holben, B. N.: Operational remote sensing of tropospheric aerosol over land from EOS moderate resolution imaging spectroradiometer, J. Geophys. Res., 102, 17051–17067, 1997.

Laurent, B., Marticorena, B., Bergametti, G., and Mei, F.: Modeling mineral dust emissions from Chinese and Mongolian deserts, Global Planet. Change, 52, 121–141, 2006.

Modeling a typical winter-time dust event

S. Kalenderski et al.

Title Page

Abstract	Introduction
Conclusions	References
Tables	Figures

◀ ▶

◀ ▶

Back Close

Full Screen / Esc

Printer-friendly Version

Interactive Discussion

Li, F. and Ramanathan, V.: Winter to summer monsoon variation of aerosol optical depth over the tropical Indian Ocean, J. Geophys. Res., 107, 4284, doi:10.1029/2001JD000949, 2002.

Liao, H. and Seinfeld, J. H.: Radiative forcing by mineral dust aerosols: sensitivity to key variables, J. Geophys. Res., 103, 31637–31646, doi:10.1029/1998JD200036, 1998.

Lin, Y. L., Farley, R. D., and Orville, H. D.: Bulk parameterization of the snow field in a cloud model, J. Climate Appl. Meteor., 22, 1065–1092, 1983.

Liu, J., Zheng, Y., Li, Z., Flynn, C., Welton, E. J., and Cribb, M.: Transport, vertical structure and radiative properties of dust events in southeast China determined from ground and space sensors, Atmos. Environ., 45, 6469–6480, doi:10.1016/j.atmosenv.2011.04.031, 2011.

Mallet, M., Tulet, P., Serça, D., Solmon, F., Dubovik, O., Pelon, J., Pont, V., and Thouron, O.: Impact of dust aerosols on the radiative budget, surface heat fluxes, heating rate profiles and convective activity over West Africa during March 2006, Atmos. Chem. Phys., 9, 7143–7160, doi:10.5194/acp-9-7143-2009, 2009.

Miller, R. L., Tegen, I., and Perlwitz, J.: Surface radiative forcing by soil dust aerosols and the hydrologic cycle, J. Geophys. Res.,109, D04203, doi:10.1029/2003JD004085, 2004.

McFarlane, S. A., Kassianov, E. I., Barnard, J., Flynn, C., and Ackerman, T. P.: Surface shortwave aerosol radiative forcing during the Atmospheric Radiation Measurement Mobile Facility deployment in Niamey, Niger, J. Geophys. Res., 114, D00E06, doi:10.1029/2008JD010491, 2009.

McKeen, S. A., Wotawa, G., Parrish, D. D., Holloway, J. S., Buhr, M. P., Hubler, G., Fehsenfeld, F. C., and Meagher, J. F.: Ozone production from Canadian wildfires during June and July of 1995, J. Geophys. Res., 107, 4192, doi:10.1029/2001JD000697, 2002.

McKendry, I. G., Strawbridge, K. B., O'Neill, N. T., Macdonald, A. M., Liu, P. S. K., Leaitch, W. R., Anlauf, K. G., Jaegle, L., Fairlie, T. D., Westphal, D. L.: Trans-Pacific transport of Saharan dust to Western North America: a case study, J. Geophys. Res., 112, D01103, doi:10.1029/2006JD007129, 2007.

Mlawer, E. J., Taubman, S. J., Brown, P. D., Iacono, M. J., and Clough, S. A.: RRTM, a validated correlated-k model for the longwave, J. Geophys. Res., 102, 16663–16682, 1997.

Osborne, S. R., Johnson, B. T., Haywood, J. M., Baran, A. J., Harrison, A. J., and McConnell, C. L.: Physical and optical properties of mineral dust aerosol during the Dust and Biomass-burning Experiment, J. Geophys. Res., 113, D00C03, doi:10.1029/2007JD009551, 2008.

Title Page

Abstract | Introduction

Conclusions | References

Tables | Figures

◄ | ►►

◄ | ►

Back | Close

Full Screen / Esc

Printer-friendly Version

Interactive Discussion

Papayannis, A., Balis, D., Amiridis, V., Chourdakis, G., Tsaknakis, G., Zerefos, C., Castanho, A. D. A., Nickovic, S., Kazadzis, S., and Grabowski, J.: Measurements of Saharan dust aerosols over the Eastern Mediterranean using elastic backscatter-Raman lidar, spectrophotometric and satellite observations in the frame of the EARLINET project, Atmos. Chem. Phys., 5, 2065–2079, doi:10.5194/acp-5-2065-2005, 2005.

Prospero, J. M., Ginoux, P., Torres, O., Nicholson, S. E., and Gill, T. E.: Environmental characterization of global sources of atmospheric soil dust identified with the Nimbus 7 Total Ozone Mapping Spectrometer (TOMS) absorbing aerosol product, Rev. Geophys., 40, 2-1–2-31, 2002.

Randerson, J. T., Van der Werf, G. R., Giglio, L., Collatz, G. J., and Kasibhatla., P. S.: Global Fire Emissions Database, Version 2 (GFEDv2.1), available at: http://daac.ornl.gov/ from Oak Ridge National Laboratory Distributed Active Archive Center, Oak Ridge, Tennesse, USA, doi:10.3334/ORNLDAAC/849 (last access: October 2012), 2005.

Remer, L. A., Kleidman, R. G., Levy, R. C., Kaufman, Y. J., Tanre, D., Mattoo, S., Martins, J. V., Ichoku, C., Koren, I., Yu, H., and Holben, B. N.: Global aerosol climatology from the MODIS satellite sensors, J. Geophys. Res., 113, doi:10.1029/2007JD009661, 2008.

Salomonson, V., Barnes, W., Maymon, P., Montgomery, H., and Ostrow, H.: MODIS: Advanced facility instrument for studies of the Earth as a system, IEEE Trans. Geosci. Remote Sens., 27, 145–153, 1989.

Santese, M., De Tomasi, F., and Perrone, M. E.: Moderate Resolution Imaging Spectroradiometer (MODIS) and Aerosol Robotic Network (AERONET) retrievals during dust outbreaks over the Mediterranean, J. Geophys. Res., 112, D18201, doi:10.1029/2007JD008482, 2007.

Satheesh, K. and Moorthy, K. K.: Radiative effects of natural aerosols: A review, Atmos. Environ., 39, 2089–2110, 2005.

Satheesh, S. K., Moorthy, K. K., Kaufman, Y. J., and Takemura, T.: Aerosol optical depth, physical properties and radiative forcing over the Arabian Sea, Meteorol. Atmos. Phys., 91, 45–62, doi:10.1007/S00703-004-0097-4, 2006.

Schell, B., Ackermann, I. J., Hass, H., Binkowski, F. S., and Ebel, A.: Modeling the formation of secondary organic aerosol within a comprehensive air quality modeling system, J. Geophys. Res., 106, 28275–28293, 2001.

Seinfeld, J. H., Carmichael, G., Arimoto, R., Conant, W. C., Brechtel, F. J., Bates, T. S., Cahill, T. A., Clarke, A. D., Doherty, S. J., Flatau, F. J., Huebert, B. J., Kim, J., Markowicz, K. M., Quinn, P. K., Russell, L. M., Russell, P. B., Shimizu, A., Shinozuka, Y., Song, C. H.,

Modeling a typical winter-time dust event

S. Kalenderski et al.

Title Page

Abstract	Introduction
Conclusions	References
Tables	Figures

◄◄   ►►

◄   ►

Back   Close

Full Screen / Esc

Printer-friendly Version

Interactive Discussion

Tang, Y., Uno, I., Vogelmann, A. M., Weber, R. J., Woo, J., and Zhang, X. Y.: ACE-ASIA, Regional climatic and atmospheric chemical effects of Asian dust and pollution, Bull. Amer. Meteor. Soc., 85, 367–380, 2004.

Skamarock, W. C., Klemp, J. B., Dudhia, J., Gill, D. O., Barker, D. M., Wang, W., and Powers, J. G.: A description of the advanced research WRF version 2, NCAR Tech. Note, NCAR/TN-468+STR, Natl. Cent. for Atmos. Res., Boulder, Colo, available at: http://wrf-model.org/wrfadmin/publications.php (last access: October 2012), 8 pp., 2008.

Slingo, A., Ackerman, T. P., Allan, R. P., Kassianov, E. I., McFarlane, S. A., Robinson, G. J., Barnard, J. C., Miller, M. A., Harries, J. E., Russell, J. E., and Dewitte, S.: Observations of the impact of a major Saharan dust storm on the atmospheric radiation balance, Geophys. Res. Lett., 33, L24817, doi:10.1029/2006GL027869, 2006.

Stockwell, W. R., Middleton, P., and Chang, J. S.: The second generation regional acid deposition model chemical mechanism for regional air quality modeling, J. Geophys. Res., 95, 16343–16367, 1990.

Tanre, D., Kaufman, Y. J., Herman, M., and Mattoo, S., Remote sensing of aerosol properties over oceans using the MODIS/EOS spectral radiances, J. Geophys. Res., 102, 16971–16988, doi:10.1029/96JD03437, 1997.

Tegen, I., Zender, C. S., and Miller, R.,: Quantifying mineral dust mass budgets: terminology, constraints, and current estimates, Eos, 85, p. 509, doi:10.1029/2004EO480002, 2004.

Watson, A. J., Bakker, D. C. E., Ridgwell, A. J., Boyd, P. W., and Law, C. S.: Effect of iron supply on Southern Ocean CO_2 uptake and implications for glacial atmospheric CO_2, Nature, 407, 730–733, 2000.

Zhang, J., Liu, S. M., Lu, X., and Huang, W. W.: Characterizing Asian wind-dust transport to the Northwest Pacific Ocean. Direct measurements of the dust flux for two years, Tellus B, 45, 335–345, doi:10.1034/j.1600-0889.1993.t01-3-00003.x, 1993.

Zhang, X. Y., Arimoto, R., and An, Z. S.: Dust emission from Chinese desert sources linked to variations in atmospheric circulation, J. Geophys. Res., 102, 28041–28047, 1997.

Zhang Y., Duliere, V., Mote, P. W., and Salathe Jr., E. P.: Evaluation of WRF and HadRM Mesoscale Climate Simulations over the U. S. Pacific Northwest, J. Climate, 22, 5511–5526, doi:10.1175/2009JCLI2875.1, 2009.

Zhao, C., Liu, X., Leung, L. R., Johnson, B., McFarlane, S. A., Gustafson Jr., W. I., Fast, J. D., and Easter, R.: The spatial distribution of mineral dust and its shortwave radiative forcing over

Title Page

Abstract	Introduction
Conclusions	References
Tables	Figures

|◄ | ►|

| ◄ | ► |

Back | Close

Full Screen / Esc

Printer-friendly Version

Interactive Discussion

North Africa: modeling sensitivities to dust emissions and aerosol size treatments, Atmos. Chem. Phys., 10, 8821–8838, doi:10.5194/acp-10-8821-2010, 2010.

Zhao, C., Liu, X., Ruby Leung, L., and Hagos, S.: Radiative impact of mineral dust on monsoon precipitation variability over West Africa, Atmos. Chem. Phys., 11, 1879–1893, doi:10.5194/acp-11-1879-2011, 2011.

Zhao, C., Liu, X., and Leung, L. R.: Impact of the Desert dust on the summer monsoon system over Southwestern North America, Atmos. Chem. Phys., 12, 3717–3731, doi:10.5194/acp-12-3717-2012, 2012.

Title Page

Abstract | Introduction

Conclusions | References

Tables | Figures

◀ | ▶

◀ | ▶

Back | Close

Full Screen / Esc

Printer-friendly Version

Interactive Discussion
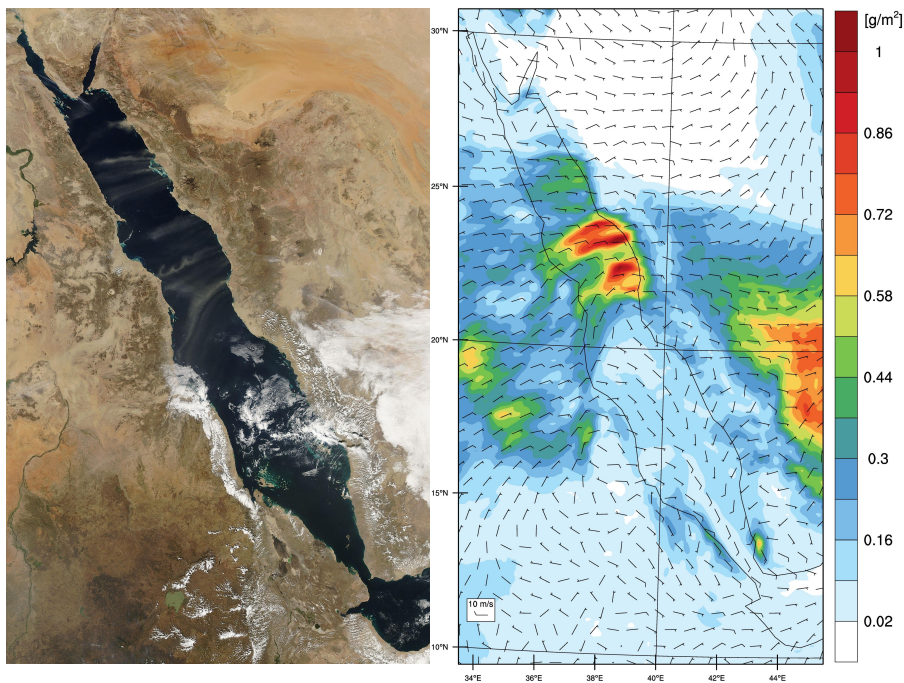
Fig. 1. An image taken by Aqua/MODIS over the Red Sea at 10:55 UTC on 14 January (left panel) and the WRF-Chem's column integrated dust load (gm^{-2}) prediction and 10 m wind vector fields for 11:00 UTC 14 January (right panel).
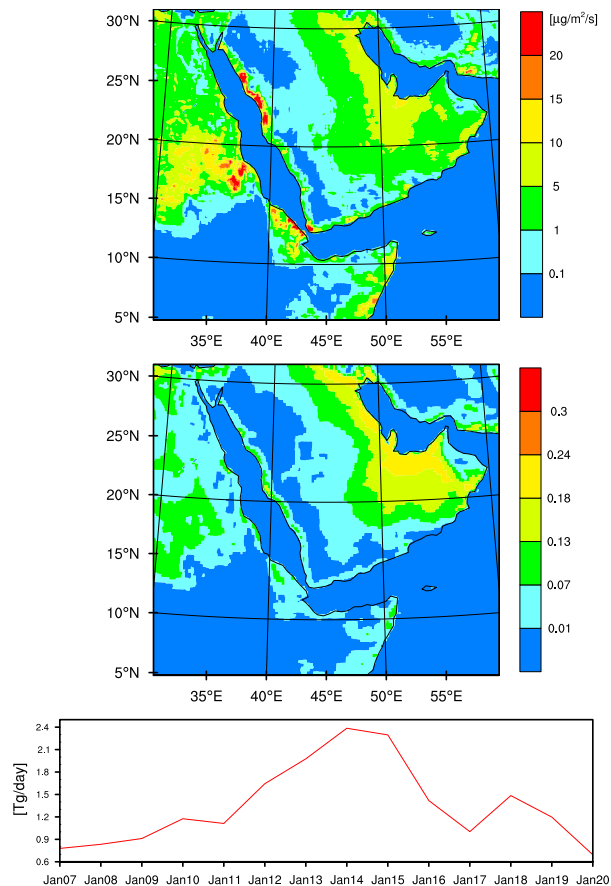
Fig. 2. Averaged for the simulation period of 7–20 January 2009 dust emissions $\mu g\,m^{-2}\,s^{-1}$ (top), source function (middle), and daily dust emissions ($Tg\,day^{-1}$) (bottom).
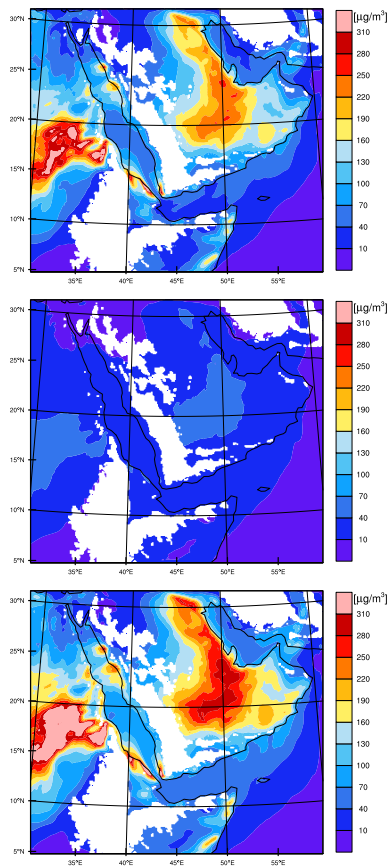
Fig. 3. Daytime (07:00–14:00 UTC) mean spatial distributions of the dust mass concentration ($\mu g\,m^{-3}$) fields in the lower atmosphere during the simulation period: coarse mode (top panel), accumulation mode (middle panel), and total concentrations (bottom panel).

Modeling a typical winter-time dust event

S. Kalenderski et al.

Title Page

Abstract | Introduction

Conclusions | References

Tables | Figures

|◄ | ►|

◄ | ►

Back | Close

Full Screen / Esc

Printer-friendly Version

Interactive Discussion
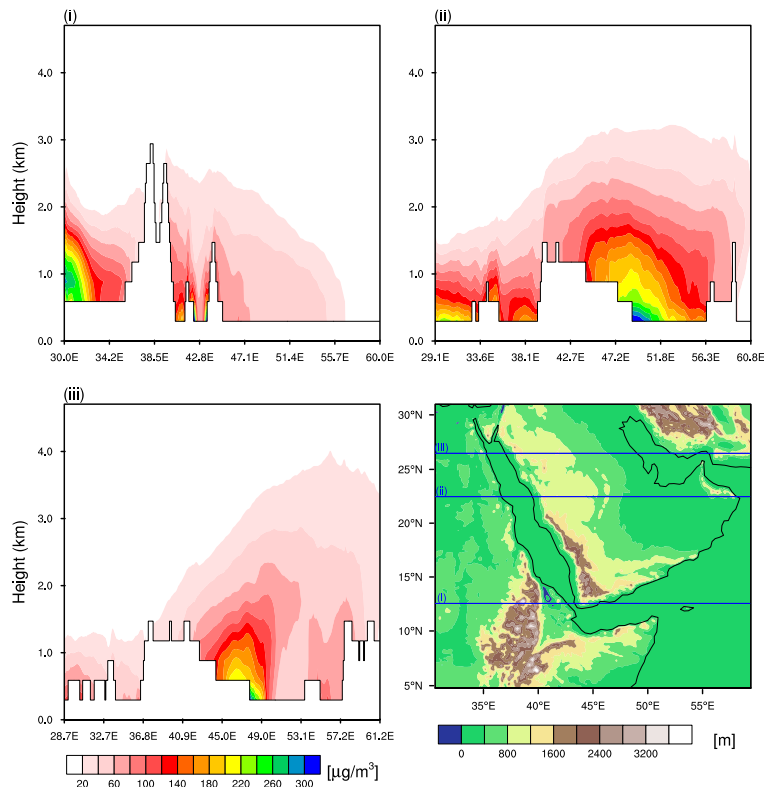
Fig. 4. Three vertical cross-sections of the averaged dust mass concentration field ($\mu g \, m^{-3}$) (top left, right, and bottom left panels) and their location on geographical map (m) (bottom right panel).
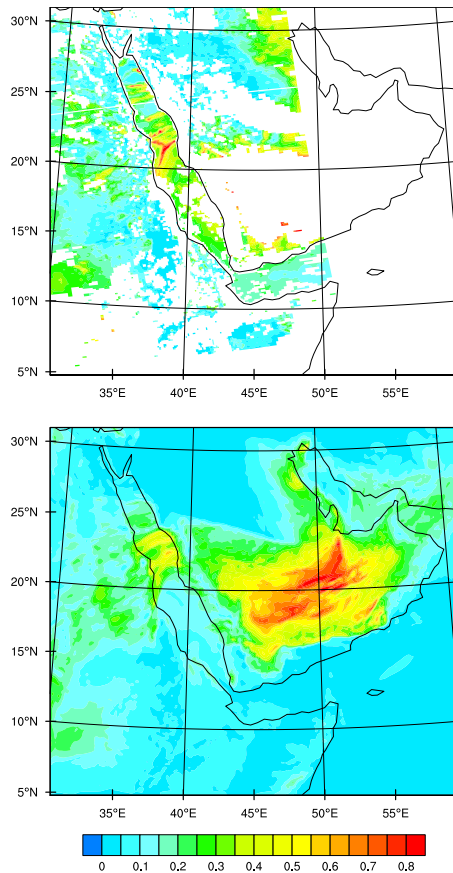
Fig. 5. Simulated AOD (600 nm, bottom panel) at 11:00 UTC on 14 January 2009 and observed AOD (550 nm, upper panel) combined from two MODIS retrievals at 10:00 and 10:55 UTC on 14 January 2009. The MODIS AOD is obtained using the standard ocean and "Deep Blue" products.

Title Page

Abstract | Introduction

Conclusions | References

Tables | Figures

◄ | ►◄

◄ | ►

Back | Close

Full Screen / Esc

Printer-friendly Version

Interactive Discussion

CC BY
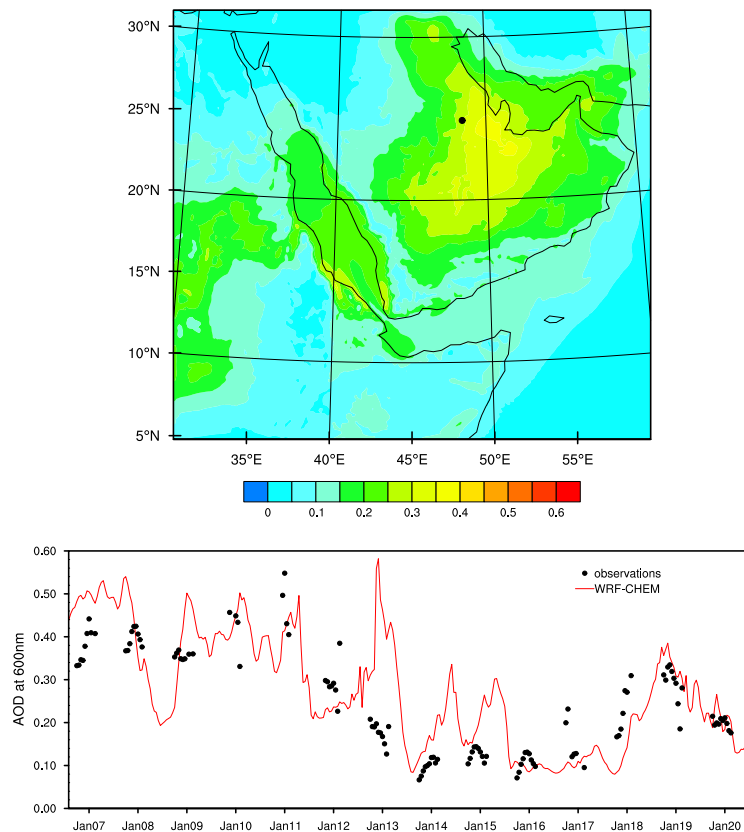
Fig. 6. Mean daytime (08:00–14:00 UTC) spatial distributions of the simulated AOD at 600 nm during the simulation period (upper panel). The black dot in the upper panel indicates the location of the AERONET Solar Village site. The lower panel shows the time series of the observed and simulated AOD at 600 nm.

Modeling a typical winter-time dust event

S. Kalenderski et al.

Title Page

Abstract | Introduction

Conclusions | References

Tables | Figures

◄ | ►

◄ | ►

Back | Close

Full Screen / Esc

Printer-friendly Version

Interactive Discussion

Full Screen / Esc

Printer-friendly Version

Interactive Discussion
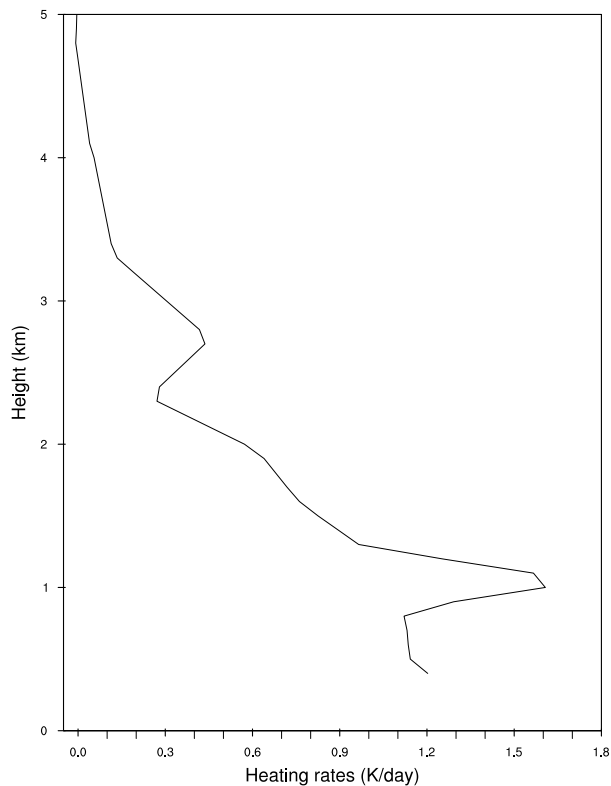
Fig. 7. Dust-induced perturbations of solar heating rates ($K\,day^{-1}$) in atmosphere over the AERONET Solar Village site at 10:00 UTC averaged over the simulation period of 7–20 January 2009.

Fig. 8. Clear sky daily averaged SW (upper row), LW (middle row), and SW + LW (lower row) radiative forcing of dust (Wm^{-2}) at the surface (left column) and at TOA (right column).
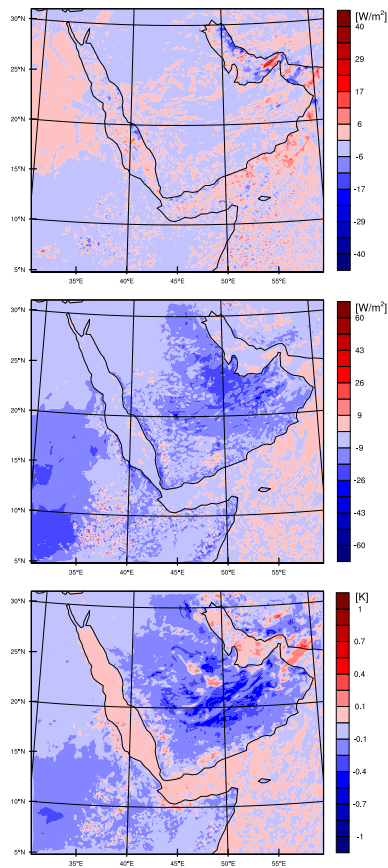
Fig. 9. Spatial distribution of dust-induced perturbations of instantaneous (at 12:00 UTC) latent heat flux (Wm^{-2}) (upper panel), sensible heat flux (Wm^{-2}) (middle panel), and air temperature at two-meter altitude (K) (lower panel) averaged over the simulation period of 7–20 January 2009.
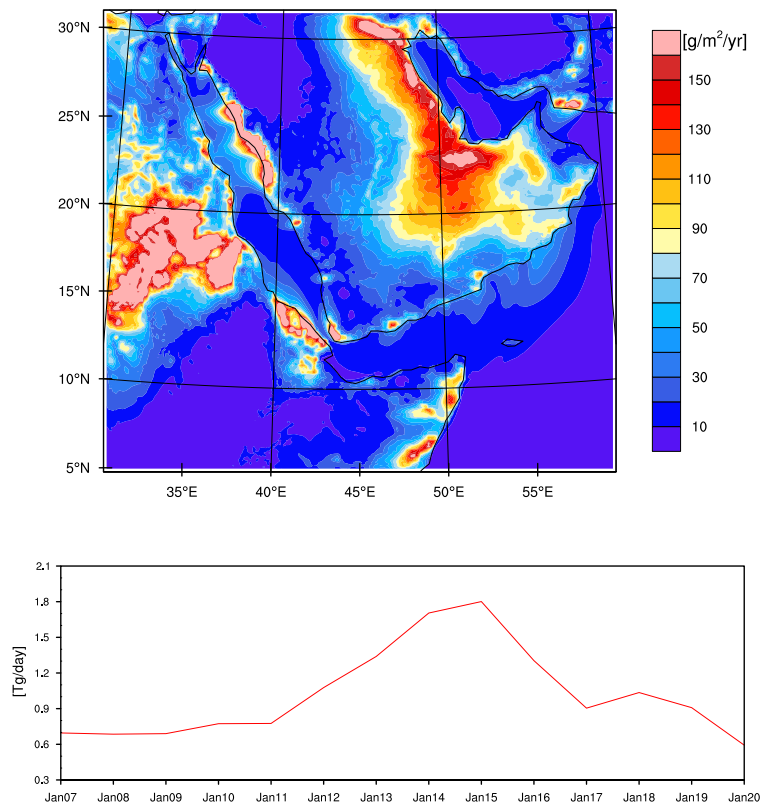
Fig. 10. The mean spatial distribution of yearly dust deposition rates ($\mathrm{g\,m^{-2}\,yr^{-1}}$) (upper panel) and a time series of the daily dust deposition in the study region (lower panel) during the period of simulations of 7–20 January 2009.

Modeling a typical winter-time dust event

S. Kalenderski et al.

Title Page

Abstract | Introduction

Conclusions | References

Tables | Figures

◄ | ►

Back | Close

Full Screen / Esc

Printer-friendly Version
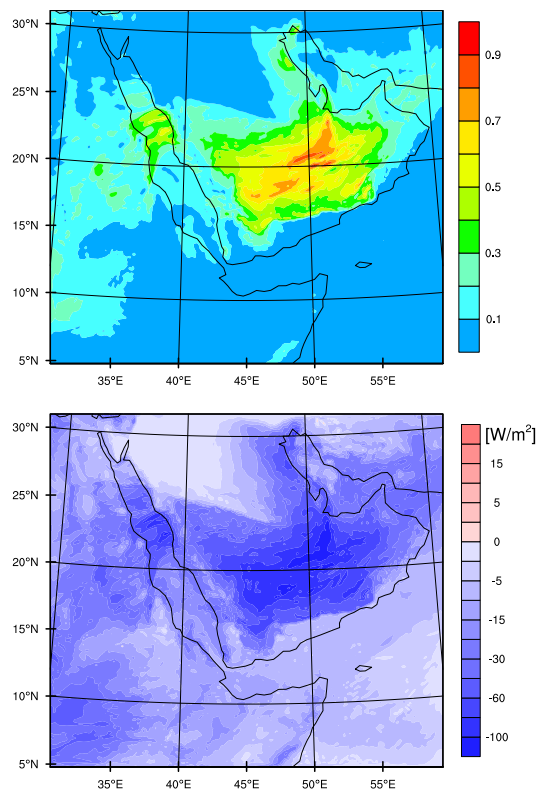
Interactive Discussion

Fig. 11. The spatial distribution of AOD (top panel) and SW radiative forcing ($W\,m^{-2}$) (bottom panel) at 11:00 UTC on 14 January 2009.